

DynaPURLS: Dynamic Refinement of Part-aware Representations for Skeleton-based Zero-Shot Action Recognition

Jingmin Zhu, Anqi Zhu, James Bailey, Jun Liu, Hossein Rahmani, Mohammed Bennamoun, Farid Boussaid, and QiuHong Ke*

Index Terms—Skeleton-Based Action Recognition, Zero-Shot Learning, Dynamic Refinement, Test-Time Adaptation, Large Language Models, Cross-Modal Alignment.

Abstract—Zero-shot skeleton-based action recognition (ZS-SAR) is fundamentally constrained by prevailing approaches that rely on aligning skeleton features with static, class-level semantics. This coarse-grained alignment fails to bridge the domain shift between seen and unseen classes, thereby impeding the effective transfer of fine-grained visual knowledge. To address these limitations, we introduce **DynaPURLS**, a unified framework that establishes robust, multi-scale visual-semantic correspondences and dynamically refines them at inference time to enhance generalization. Our framework leverages a large language model to generate hierarchical textual descriptions that encompass both global movements and local body-part dynamics. Concurrently, an adaptive partitioning module produces fine-grained visual representations by semantically grouping skeleton joints. To fortify this fine-grained alignment against the train-test domain shift, DynaPURLS incorporates a dynamic refinement module. During inference, this module adapts textual features to the incoming visual stream via a lightweight learnable projection. This refinement process is stabilized by a confidence-aware, class-balanced memory bank, which mitigates error propagation from noisy pseudo-labels. Extensive experiments on three large-scale benchmark datasets, including NTU RGB+D 60/120 and PKU-MMD, demonstrate that DynaPURLS significantly outperforms prior art, setting new state-of-the-art records. The source code is made publicly available at <https://github.com/Alchemist0754/DynaPURLS>

1 INTRODUCTION

HUMAN Action Recognition (HAR) has emerged as a cornerstone technology in computer vision, enabling machines to comprehend human behaviors from sensory data. This capability is fundamental to transformative applications across diverse domains, including immersive virtual reality [1], [2], intelligent transportation [3], [4], large-scale video retrieval [5], and human-robot collaboration [6], [7]. While RGB-based solutions have historically dominated HAR research, buoyed by massive annotated datasets [8], [9], the maturation of human pose estimation [10] and depth-sensing hardware [11], [12] has positioned 3D skeleton sequences as a compelling alternative. Skeleton data offers distinct advantages: it is computationally efficient, inherently privacy-preserving, and robust to environmental variations such as background clutter and lighting changes [13], [14], [15].

Despite remarkable progress in fully supervised skeleton-based HAR [16], [17], [18], [19], [20], [21], these approaches are constrained by their reliance on exhaustive annotations for all action classes. This paradigm falters when confronted with real-world scenarios involving rare, hazardous, or

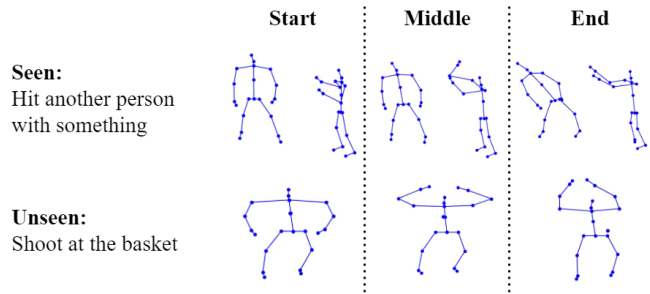


Fig. 1: An example illustrating the limitations of global-only alignment. A seen class (“Hit another person with something”) and an unseen class (“Shoot at the basket”) from *NTU-RGB+D 120* [12] exhibit different overall motions but share similar local hand movements. Effective knowledge transfer in ZSL requires capturing such fine-grained, part-level similarities.

expensive-to-collect actions, creating a critical deployment bottleneck. Zero-Shot Learning (ZSL) offers a compelling path forward by transferring knowledge from seen to unseen categories through a shared semantic space, enabling the recognition of novel actions without direct training examples.

However, existing skeleton-based ZSL methods [23], [24], [25] predominantly depend on aligning a single, global motion feature with a corresponding class-level semantic embedding. This coarse alignment strategy is insufficient for the nuanced demands of action recognition. As illustrated in Figure 1, actions with disparate global patterns (e.g., “Hit another person with something” vs. “Shoot at the basket”) may share remarkably similar fine-grained motions

• *J. Zhu and A. Zhu are with Monash University.
E-mail: jingmin.zhu1@monash.edu, maggie.zhu@monash.edu*

• *J. Bailey is with University of Melbourne.
E-mail: baileyj@unimelb.edu.au*

• *H. Rahmani and J. Liu are with Lancaster University.
E-mail: h.rahmani@lancaster.ac.uk, j.liu81@lancaster.ac.uk*

• *M. Bennamoun and F. Boussaid are with University of Western Australia.
E-mail: mohammed.bennamoun@uwa.edu.au, farid.boussaid@uwa.edu.au*

• *Q. Ke is with Monash University.
E-mail: QiuHong.Ke@monash.edu*

* Corresponding author.

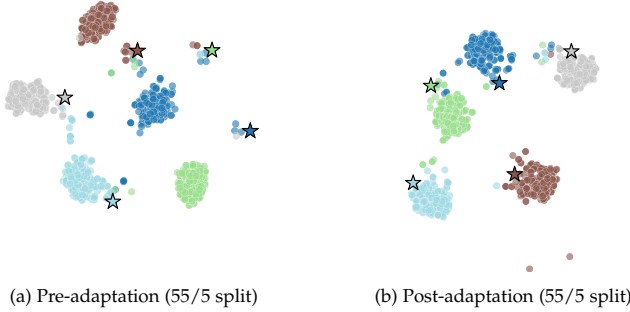


Fig. 2: t-SNE visualization of feature distributions before and after test-time feature refinement. Subfigures (a) and (b) illustrate the feature distributions on the test data of NTU RGB+D 60 [22] 55/5 split before and after test-time refinement, where \star represents text features and \bullet represents skeleton features, with different colors denoting distinct classes. The results demonstrate that our method effectively promotes the alignment between text and skeleton features and enhances classification discriminability, leading to a significant 9.3% improvement in classification performance.

in specific body parts. Such part-level correspondences are a crucial source of transferable knowledge, yet they are largely neglected by current models. Moreover, even recent fine-grained ZSL methods [26], [27] introduce another critical challenge by operating on static semantic information. The textual descriptions are generated offline from language prompts alone, without access to the visual data they are meant to represent. This often results in descriptions that are semantically plausible but lack the subtle, instance-specific distinctions necessary for precise recognition. The learned alignment is often brittle and fails to generalize, as the features of unseen actions introduce a significant domain shift, preventing effective knowledge transfer.

To overcome these interconnected challenges, we introduce **DynaPURLS**, a framework that pioneers a paradigm shift from static matching to dynamic, adaptive alignment. To address the issue of coarse alignment, DynaPURLS forges a more granular connection between semantics and motion. It employs a Large Language Model (LLM), specifically GPT-3 [28], to decompose high-level action labels into detailed descriptions of both global movements and localized part-level motions. These multi-granularity descriptions, encoded via text encoders like CLIP [29], are then aligned with corresponding visual features. Critically, instead of using fixed body parts, DynaPURLS utilizes an adaptive partitioning module that learns to group skeleton joints, creating visual representations that dynamically match the generated semantic descriptions. This ensures a robust, fine-grained alignment during training.

Furthermore, DynaPURLS tackles the problem of static semantics by introducing a **dynamic, confidence-guided refinement at inference time**. This novel mechanism directly addresses the domain shift problem by introducing a lightweight transformation that dynamically refines the fine-grained textual features to adapt to the specific visual context of each sample. This refinement markedly enhances alignment and modality coherence for unseen classes, as visualized in Figure 2. To ensure a stable optimization process and mitigate bias, our methodology is fundamentally architected on a principle of **class-balancing**. The core

of this is a **confidence-guided optimization strategy** that leverages the model's own high-confidence predictions as a self-supervised signal. We innovate by incorporating a small-scale, **class-balanced memory bank** to mechanistically avert the risk of overconfidence. This design filters and stores high-confidence samples, enforcing a balanced representation across classes during updates, which not only prevents model skew but also **drastically improves the recognition rate of previously misclassified minority classes**.

In summary, our main contributions are:

- We propose **DynaPURLS**, a novel framework for zero-shot skeleton-based action recognition that addresses the limitations of coarse alignment and static semantics by creating a dynamic link between visual and textual features.
- We introduce a **fine-grained adaptive alignment** strategy that matches multi-granularity semantics from an LLM with visual features from a novel **adaptive partitioning module** to enable effective part-level knowledge transfer.
- We pioneer a **test-time feature refinement** mechanism using a lightweight, **confidence-guided optimization** and a **class-balanced memory bank** to adapt semantic features at inference, mitigating domain shift with minimal overhead.
- Through extensive experiments on three challenging benchmarks (NTU RGB+D 60 [11], NTU RGB+D 120 [12], and PKU-MMD [30]), we demonstrate that DynaPURLS sets a new **state of the art** in both ZSL and GZSL settings.

This paper is an extension of our earlier conference paper [31]. The main improvements are: (1) A new dynamic refinement module for inference time that fixes the static semantic problems of the original PURLS and gives clear performance gains. As far as we know, this is the first work to use test-time adaptation for zero-shot skeleton-based action recognition. (2) We add an evaluation in the GZSL setting and show that our method achieves state-of-the-art results, outperforming PURLS and other previous methods. (3) A set of detailed ablation studies is provided to analyze each part of our dynamic model, explaining our design choices and showing their effectiveness.

2 RELATED WORK

2.1 Multi-modal Learning and Zero-Shot Foundations

Zero-Shot Learning (ZSL) seeks to endow models with the ability to recognize novel classes by transferring knowledge from seen classes via a shared semantic space, typically informed by textual descriptions or attributes. Early embedding-based methods focused on learning a compatible projection of visual and semantic data into a common space and optimizing a distance metric [32], [33], [34]. This paradigm was advanced by generative approaches, which learn to synthesize visual features from semantic embeddings, thereby creating prototypes for unseen classes and alleviating the bias towards seen categories [35]. Further inspired by human cognition, some methods proposed disentangling representations into local, attribute-like concepts to improve compositional generalization [36], [37]. The

modern ZSL landscape has been reshaped by large-scale multi-modal representation learning. The introduction of CLIP [29], which contrastively pre-trains on massive image-text pairs from the web, created a powerful and universal vision-language manifold that now serves as a foundational backbone for countless downstream tasks. This success has spurred efforts to extend this alignment to other modalities. For instance, ULIP [38] and Point-CLIP [39] successfully unified 3D point cloud representations with the image-text space, demonstrating that knowledge distilled from the rich vision-language manifold can effectively address data scarcity in other domains.

Our work builds upon these foundational principles of cross-modal alignment. However, we contend that the direct application of these general-purpose models to skeleton-based action recognition is suboptimal. The unique, structured, and temporal nature of skeleton data necessitates specialized architectural designs to fully exploit the modality's fine-grained spatio-temporal characteristics, a challenge that generic vision-language models are not inherently equipped to handle.

2.2 Zero-Shot Learning for Skeleton-Based Actions

Adapting ZSL principles to skeleton-based action recognition began with pioneering works that projected globally-pooled skeleton features into a semantic space using DeViSE-like models or common-space metric learning [23], [40]. While these methods validated the feasibility of skeleton ZSL, they were limited by their reliance on coarse, global representations, often failing to distinguish actions with similar overall movements but different local limb motions. Subsequent research has progressively sought more fine-grained alignment. For instance, SMIE [25] improved temporal modeling by maximizing the mutual information between visual and textual distributions, while SynSE-ZSL [24] made an early attempt at local semantic matching by leveraging the syntactic structure (verbs and nouns) within action labels to guide knowledge transfer. The field took a significant leap forward with the use of Large Language Models (LLMs) to generate rich, multi-granularity semantic descriptions. Our foundational work, **PURLS** [31], and the concurrent **STAR** [27], represent the state of the art by aligning fine-grained, spatio-temporal skeleton features with detailed, LLM-generated prompts, proving the efficacy of multi-level cross-modal alignment.

Despite their increasing sophistication, these frameworks, including our own **PURLS**, have largely been built upon **static semantic representations**. Recognizing this limitation, the most recent works have begun to challenge this static paradigm during the model training phase. For example, SCoPLe [41] introduces learnable cross-modal prompts to refine semantic guidance, and Neuron [42] proposes a context-aware evolving representation. While these methods embed adaptability into the training process, the learned semantic anchors remain fixed during inference. This still leaves a critical "Semantic-Visual Gap" when encountering the dynamic visual manifestations of unseen classes. Our work addresses this gap from a distinct angle, proposing a method to overcome the static representation problem directly at **inference-time**, thereby tackling the domain shift inherent in ZSL more effectively.

2.3 Test-Time Adaptation for Zero-Shot Learning

Test-Time Adaptation (TTA) aims to bridge the distribution gap between training and test data by adapting a pre-trained model during inference [43], [44], [45], [46]. These general-purpose methods were not designed for the unique challenges of skeleton-based ZSL. Many approaches adapt the model using pseudo-labels derived from its own confident predictions, for instance by minimizing prediction entropy or using nearest-neighbor classification [47]. A prominent trend in vision-language models involves adapting textual prompts to better match test data, using augmentation-based consistency [48], diffusion model-based augmentations [49], or other prompt enhancement strategies [50]. Other efficient methods directly refine predictions by aligning test feature distributions or constructing feature caches [51]. However, when applied to skeleton ZSL, these generic strategies fall short. They either incur significant computational overhead or treat features holistically, failing to perform the fine-grained, targeted adjustments needed to bridge the specific "Semantic-Visual Gap" between static, multi-level textual prompts and dynamic skeleton motions.

To address this specific challenge, we propose **DynaPURLS**, a novel TTA strategy deeply integrated with our **PURLS** backbone. Rather than applying a generic adaptation scheme, **DynaPURLS** is purpose-built to resolve the core limitation of **PURLS**: its reliance on static semantic representations. Its core novelty is being the first to propose adapting the **multi-granularity semantic representations themselves** at test time. This is achieved through a lightweight, gradient-guided online optimization that transforms semantic features to align with incoming visual evidence, avoiding costly updates to the large visual and text encoders. This dynamic refinement is stabilized by a confidence-guided optimization mechanism and a class-balanced memory bank, ensuring robust and efficient adaptation tailored to the structured nature of skeleton data. **DynaPURLS** thus carves a distinct path by showing that a specialized, semantics-focused adaptation is significantly more effective for skeleton-based ZSL.

3 METHODOLOGY

In this section, we introduce our novel framework, the **Dynamic Part-aware Unified Representation between Language and Skeleton (DynaPURLS)**, designed for zero-shot skeleton-based action recognition. As shown in Fig. 3 and Fig. 6, the framework contains a multi-granularity semantic representation module, which leverages Large Language Models (LLMs) to generate rich, hierarchical action descriptions that capture transferable motion primitives; an adaptive partitioning and visual-semantic alignment module, which employs a cross-modal attention mechanism to dynamically align visual features with their corresponding semantic concepts, overcoming the limitations of static partitioning; and a dynamic test-time feature refinement module, which adapts the semantic embeddings online using a confidence-guided, class-balanced memory bank for robust handling of domain shifts inherent to unseen classes. We first describe the problem definition (Section 3.1) before detailing each component: the multi-granularity semantic representation (Section 3.2), the adaptive partitioning and visual-semantic

alignment (Section 3.3), and the dynamic test-time feature refinement (Section 3.4).

3.1 Problem Definition

Zero-Shot Learning (ZSL). The task of Zero-Shot Learning (ZSL) [52] aims to enable models to recognize instances from classes that were not present during training. Formally, we are given a labeled training dataset $\mathcal{D}_s = \{(\mathbf{x}_i, y_i)\}_{i=1}^{N_s}$ from a set of *seen* classes \mathcal{Y}_s , where $\mathbf{x}_i \in \mathcal{X}$ represents a visual input (in our case, a skeleton sequence), and $y_i \in \mathcal{Y}_s$ is its corresponding class label. The core challenge lies in enabling the model to correctly classify samples from a disjoint set of *unseen* classes \mathcal{Y}_u during inference, where $\mathcal{Y}_s \cap \mathcal{Y}_u = \emptyset$.

This cross-class generalization is made possible through a shared semantic space that bridges the gap between visual features and class concepts. Typically, this takes the form of pre-defined vector embeddings $\mathbf{F} = \{F_y \in \mathbb{R}^d : y \in \mathcal{Y}_s \cup \mathcal{Y}_u\}$, which are available for all classes (both seen and unseen). These embeddings encode semantic properties that are expected to correlate with visual characteristics. In the standard ZSL setting, the model is evaluated on a test set $\mathcal{D}_u = \{(\mathbf{x}_j, y_j)\}_{j=1}^{N_u}$ where $y_j \in \mathcal{Y}_u$, and the prediction space is restricted to unseen labels, i.e., $f : \mathcal{X} \rightarrow \mathcal{Y}_u$.

Generalized Zero-Shot Learning (GZSL). While standard ZSL provides a useful theoretical framework, real-world applications often demand a more challenging setting known as Generalized ZSL (GZSL). In this setting, the test set contains samples from both seen and unseen classes, and the prediction space is expanded to the union of both label sets, $f : \mathcal{X} \rightarrow \mathcal{Y}_s \cup \mathcal{Y}_u$. This introduces a significant challenge: the model must not only correctly classify novel unseen actions but also maintain its ability to recognize seen actions it was trained on. Many ZSL approaches suffer from a strong bias towards seen classes in this setting, as the model has learned direct mappings for these classes during training, leading to a tendency to misclassify unseen samples as belonging to familiar seen categories.

Test-Time Adaptation (TTA). Test-Time Adaptation (TTA) [44], [53] represents a paradigm shift in how models handle distribution shifts between training and testing data. Rather than relying solely on the generalization capability learned during training, TTA enables models to dynamically adapt using the test data itself, typically in an online and unsupervised manner. For an incoming mini-batch of test data $\mathcal{B}_t = \{\mathbf{x}_i\}_{i=1}^B$ at time step t , the model parameters θ are updated based on an adaptation objective $\mathcal{L}_{\text{adapt}}$:

$$\theta_t = \theta_{t-1} - \alpha \nabla_{\theta} \mathcal{L}_{\text{adapt}}(\mathcal{B}_t; \theta_{t-1}) \quad (1)$$

where α is the learning rate for adaptation. In the context of ZSL, TTA presents a particularly promising direction for bridging the gap between the training distribution $P_{\text{train}}(\mathbf{x} | y \in \mathcal{Y}_s)$ and the distinct test-time distribution $P_{\text{test}}(\mathbf{x} | y' \in \mathcal{Y}_u)$. This is especially crucial given that unseen classes may exhibit visual characteristics that differ systematically from those observed during training.

3.2 Multi-Granularity Semantic Representation Generation Module

Human action understanding inherently operates at multiple levels of granularity. When observing an action, we simul-

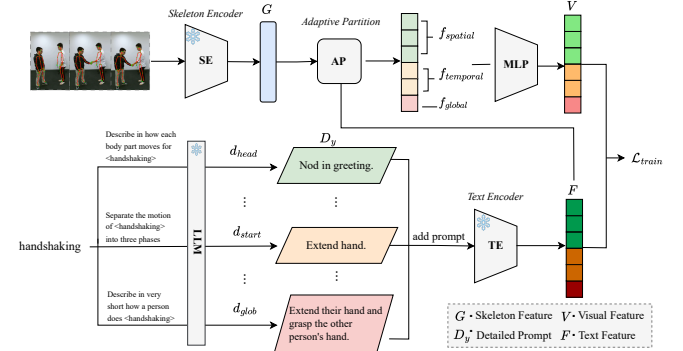


Fig. 3: **Training pipeline of DynaPURLS.** The model learns a robust static alignment between visual features extracted by the skeleton encoder and multi-granularity semantic embeddings from the text encoder. We employ a adaptive partitioning module where static text embeddings serve as queries to flexibly aggregate visual information. The entire network is optimized using a symmetric contrastive loss to align the resulting fused visual representations with their corresponding static text descriptions across all granularities.

taneously process global patterns (e.g., "a person throwing something") and local details (e.g., "the arm extends upward" or "the legs provide stability"). Inspired by this multi-scale perception, we propose to decompose actions into semantically meaningful components that can be independently learned and transferred across different action classes.

3.2.1 Fine-grained Action Decomposition

We regard an action as a specific combination of local body movements that can be spatially or temporally decomposed. Beyond label-level semantics, these local movements represent individual visual concepts that are transferable across different classes. For instance, the arm-raising motion in "shooting a basketball" shares visual similarities with the arm-raising in "hitting with an object" despite the different overall action contexts.

To systematically extract such underlying semantics, we leverage the powerful language understanding capabilities of GPT-3 to generate detailed textual descriptions for movements at different scales. We design three types of decomposition: (1) **Spatial Decomposition**, where we generate descriptions for movements performed by $P = 4$ distinct body parts: 'head', 'hands', 'torso', and 'legs', as exemplified in Table 1; (2) **Temporal Decomposition**, where we divide the action into $Z = 3$ contiguous temporal intervals: 'start', 'middle', and 'end', as shown in Table 2; and (3) **Global Description**, where we generate holistic descriptions that augment the original action labels with more detailed semantic information about the overall motion pattern.

3.2.2 Prompt Engineering and Embedding Generation

To ensure consistent and informative responses from GPT-3, we employ a structured prompt template. For local part descriptions, we format our queries as: Using the following format, <QUESTION>: <LOCAL PART 1> would: ...; <LOCAL PART 2> would: ...; ...; <LOCAL PART H> would: ... where $H \in \{P, Z\}$ represents either the number of body parts or temporal

Action	Question: Describe in very short how each body part moves for <Action>.			
	Head	Hands	Torso	Legs
Hit another person with something	Turn towards the other person.	Grip the object tightly and thrust it forward.	Twist and turn to generate momentum for the strike.	Stomp the ground to provide additional force for the strike.
Shoot at the basket	Turn and look up towards the basket.	Grip the basket and release it.	Twist and extend to generate power for the shot.	Bend slightly and propel slightly upward.

TABLE 1: Example body-part-based descriptions generated by GPT-3. The refined explanations reveal shared motion patterns between semantically related actions: both ‘Hit another person with something’ and ‘shoot at the basket’ involve similar head turning and hand gripping movements, highlighting transferable local motion concepts.

Action	Question: Separate the motion of <Action> into three phases.			Question: Describe in very short how a person does <Action>.
	Start	Middle	End	
Hit another person with something	Raise arm.	Swing arm.	Strike other person.	Swing their arm and strike the other person with the object.
Shoot at the basket	Raise arm.	Throw ball.	Aim at basket.	Raise their arm and throw the ball towards the basket.

TABLE 2: Example temporal-interval-based and global descriptions generated by GPT-3. The temporal decomposition reveals that both actions share a common starting phase (raising arm), demonstrating how temporal segments can capture transferable motion primitives across different action classes.

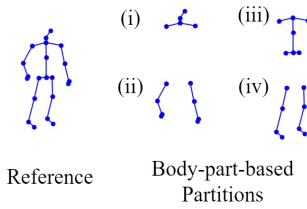


Fig. 4: Static spatial partitioning scheme for decomposing 25 body joints into four semantic body parts: (i) Head: joints 0, 1, 2, 3 (ii) Hands: joints 4-11, 21-24 (iii) Torso: joints 12, 16, 20 (iv) Legs: joints 13-15, 17-19. While intuitive, this rigid partitioning fails to capture action-specific variations in body part relevance.

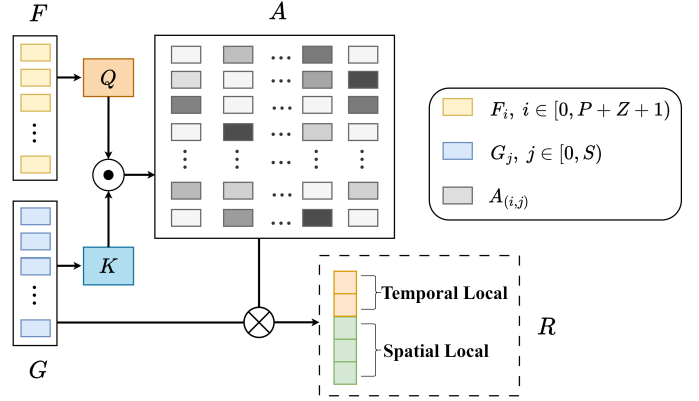


Fig. 5: Adaptive partitioning module. Each textual description acts as a query to attend over all spatio-temporal visual features, learning to focus on the most relevant nodes for that particular semantic concept. This allows flexible, context-aware feature aggregation that transcends rigid spatial or temporal boundaries.

segments. This structured format ensures that GPT-3 provides complete descriptions for all requested components in a consistent manner. The specific prompt content and outputs can be referenced in Tables 1 and 2.

After acquiring the targeted descriptions $\mathcal{D}_y = \{d_y^{(i)}\}_{i=0}^{P+Z}$ for each class y (where $d_y^{(0)}$ represents the global description and $d_y^{(1)}$ through $d_y^{(P+Z)}$ represent local descriptions), we convert them into standard visual-language prompts. Specifically, each description is wrapped in a template such as “a video of [DESCRIPTION]” to maintain consistency with the pre-training objective of the visual-language model. These prompts are then processed through a pre-trained CLIP text encoder, f_{text} , to obtain their corresponding embeddings:

$$F_y^{(i)} = f_{\text{text}}(\text{prompt}(d_y^{(i)})) \in \mathbb{R}^d \quad (2)$$

where $\text{prompt}(\cdot)$ denotes the prompting function and d is the text embedding dimension. The embeddings are concatenated to form the static multi-granularity semantic anchor matrix for all C classes:

$$\mathbf{F} = \{F_y : y \in \mathcal{Y}_s \cup \mathcal{Y}_u\} \in \mathbb{R}^{C \times (P+Z+1) \times d} \quad (3)$$

This matrix \mathbf{F} serves as the foundational semantic representation for our framework, encoding both global action concepts and local motion patterns that can be shared across different action classes.

3.3 Adaptive Partitioning and Visual-Semantic Alignment

This section details our mechanism for adaptively partitioning and aligning multi-granularity semantic representations with visual features from skeleton sequences. This approach learns a robust alignment during training, which serves as the foundation for dynamic refinement at test time.

3.3.1 Visual Feature Extraction

Given a raw skeleton sequence $\mathbf{x} \in \mathbb{R}^{L \times J \times M \times 3}$, where L, J, M are the sequence length, number of joints, and maximum number of persons, respectively, we first apply standard pre-processing (padding and normalization) following [21]. We then employ a pre-trained Shift-GCN [21] as our backbone encoder, denoted g , to extract rich spatio-temporal features:

$$\mathbf{G} = g(\mathbf{x}) \in \mathbb{R}^{S \times n} \quad (4)$$

where $S = L' \times J$ is the total number of spatio-temporal nodes (with L' being the temporal dimension after pooling), and n is the visual feature dimension. Each row in \mathbf{G} is a feature vector for a specific joint at a specific time, capturing both spatial configuration and temporal dynamics.

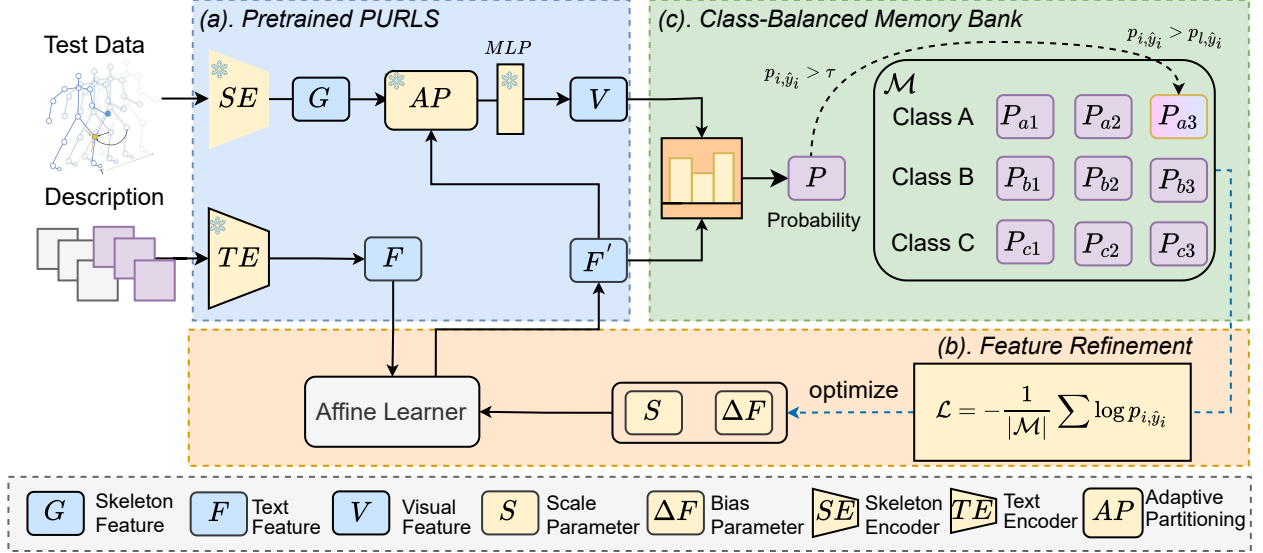


Fig. 6: **Test-time feature refinement pipeline of DynaPURLS.** The framework dynamically refines semantic embeddings based on high-confidence test samples stored in a class-balanced memory bank, enabling robust adaptation to distribution shifts in unseen classes. The refined embeddings are used to update the cross-modal attention mechanism for improved visual-semantic alignment.

3.3.2 Adaptive Partitioning via Cross-Modal Attention

To align the visual feature map \mathbf{G} with our multi-granularity text features \mathbf{F} , we require a mechanism to group visual features based on their semantic relevance to each description. A naive approach is static partitioning: manually grouping joints into pre-defined body parts (Fig. 4) and dividing the sequence into fixed temporal segments. However, this method is fundamentally flawed due to its **rigidity**, as pre-defined partitions cannot adapt to action-specific motion variations. It also leads to a **loss of context** (e.g., leg motion is best understood with concurrent arm swing) and creates **boundary issues**, where hard boundaries can unnaturally sever semantically coherent motions.

To overcome these limitations, we propose an adaptive partitioning module based on cross-modal attention, depicted in Figure 5. This approach learns to dynamically aggregate description-relevant features from the entire spatio-temporal map \mathbf{G} , allowing each semantic concept to attend to its most relevant visual evidence, irrespective of pre-defined boundaries.

Specifically, we treat the text embeddings as queries and the visual features as keys and values. The queries are learned projections of the static semantic embeddings:

$$\mathbf{Q} = \mathbf{F}\mathbf{W}_Q \in \mathbb{R}^{(P+Z+1) \times h} \quad (5)$$

where $\mathbf{W}_Q \in \mathbb{R}^{d \times h}$ is a learnable projection matrix. Similarly, the visual features are projected to form keys:

$$\mathbf{K} = \mathbf{G}\mathbf{W}_K \in \mathbb{R}^{S \times h} \quad (6)$$

where $\mathbf{W}_K \in \mathbb{R}^{n \times h}$ is another learnable projection. The attention matrix $\mathbf{A} \in \mathbb{R}^{(P+Z+1) \times S}$ is computed via scaled dot-product attention:

$$\mathbf{A} = \text{softmax} \left(\frac{\mathbf{Q}\mathbf{K}^\top}{\sqrt{h}} \right) \quad (7)$$

Intuitively, each row \mathbf{A}_i of the attention matrix represents a soft selection of all S spatio-temporal nodes with respect to the i -th textual description. The final fused visual representation $\mathbf{R} \in \mathbb{R}^{(P+Z+1) \times n}$ is obtained by a weighted aggregation of the visual features:

$$\mathbf{R} = \mathbf{A}\mathbf{G} \quad (8)$$

This attention-based fusion is **flexible**, **context-preserving**, and **learnable**, allowing it to adapt to the specific characteristics of each action class.

3.3.3 Visual-Semantic Alignment and Training Objective

The training objective is to learn a strong alignment between the fused visual representations and the static multi-granularity semantic embeddings. We project each row vector $\mathbf{r}_i \in \mathbb{R}^n$ from the fused visual representation \mathbf{R} (Eq. 8) into the textual embedding space using a trainable MLP, f_{skel} :

$$\mathbf{v}_i = f_{\text{skel}}(\mathbf{r}_i) \in \mathbb{R}^d, \quad i \in \{0, 1, \dots, P+Z\} \quad (9)$$

We employ a symmetric InfoNCE loss [54] to maximize the similarity between matched visual-text pairs while pushing negative pairs apart. The contrastive loss for a projected visual feature \mathbf{v}_i and its ground-truth text feature \mathbf{f}_i is:

$$\begin{aligned} \mathcal{L}(\mathbf{v}_i, \mathbf{f}_i) = & -\frac{1}{2} \log \frac{\exp(\text{sim}(\mathbf{v}_i, \mathbf{f}_i)/\tau)}{\sum_{o \in \mathcal{Y}_s} \exp(\text{sim}(\mathbf{v}_i, \mathbf{f}_i^o)/\tau)} \\ & -\frac{1}{2} \log \frac{\exp(\text{sim}(\mathbf{v}_i, \mathbf{f}_i)/\tau)}{\sum_{w \in \mathcal{B}} \exp(\text{sim}(\mathbf{v}_i^w, \mathbf{f}_i)/\tau)} \end{aligned} \quad (10)$$

where $\text{sim}(\cdot, \cdot)$ is cosine similarity, \mathbf{f}_i^o are text embeddings from other (negative) seen classes, \mathbf{v}_i^w are visual embeddings from other (negative) samples in the batch \mathcal{B} , and τ is a temperature parameter. The symmetric formulation ensures a robust bidirectional alignment.

The overall training loss aggregates the losses across all granularities using learnable importance weights α_i :

$$\mathcal{L}_{\text{train}}(\mathbf{x}, y) = \sum_{i=0}^{P+Z} \alpha_i \mathcal{L}(\mathbf{v}_i, \mathbf{f}_i) \quad (11)$$

These weights allow the model to adaptively balance the contribution of each semantic granularity, which is crucial as different actions rely on different scales of motion. The parameters optimized at this stage are $\theta_{\text{train}} = \{g, \mathbf{W}_Q, \mathbf{W}_K, f_{\text{skel}}, \{\alpha_i\}\}$.

3.4 Dynamic Test-Time Feature Refinement

While the alignment module establishes a robust visual-semantic mapping, the static nature of text embeddings limits performance against test-time distribution shifts, especially for unseen classes. To address this, we introduce our primary innovation: a dynamic query refinement mechanism that adapts semantic representations online. This module builds upon the cross-modal attention from Section 3.3. By refining the semantic features, which serve as queries, we indirectly yet effectively influence the visual feature aggregation, thereby dynamically adapting the final visual representations to the test distribution.

3.4.1 Dynamic Semantic Refinement

Instead of using static queries from \mathbf{F} , we introduce lightweight, learnable parameters to adjust the semantic embeddings based on test data characteristics. For each test batch, the refined text features \mathbf{F}' are computed via an affine transformation:

$$\mathbf{F}' = \mathcal{N}(\mathbf{S} \odot \mathbf{F} + \Delta \mathbf{F}) \quad (12)$$

where $\mathbf{S} \in \mathbb{R}^{C \times (P+Z+1) \times d}$ is a learnable scaling tensor, $\Delta \mathbf{F} \in \mathbb{R}^{C \times (P+Z+1) \times d}$ is a learnable bias tensor, \odot denotes element-wise multiplication, and $\mathcal{N}(\cdot)$ is per-vector L_2 normalization. This provides an effective yet efficient mechanism for adapting embeddings to the test distribution.

The test-time fusion process then uses dynamic queries constructed from these refined features:

$$\mathbf{Q}' = \mathbf{F}' \mathbf{W}_Q \quad (13)$$

The subsequent attention and feature aggregation proceed as before, but now with adaptive queries. This dynamic adjustment of semantic queries indirectly refines the fused skeleton features by altering the attention weights. Critically, during this stage, the main network parameters θ_{train} are frozen. Only the lightweight refinement parameters $\theta_{\text{adapt}} = \{\mathbf{S}, \Delta \mathbf{F}\}$ are updated, ensuring efficient refinement without catastrophic forgetting.

3.4.2 Confidence-Guided Online Optimization

The efficacy of TTA hinges on the quality of its self-supervisory signal. Naive entropy minimization often leads to confirmation bias, where the model reinforces its own incorrect predictions. To avert this, we propose a more robust strategy based on selective optimization.

Class-Balanced Memory Bank. Our key insight is that samples with high prediction confidence provide more reliable supervisory signals. We introduce a **Class-Balanced**

Algorithm 1: DynaPURLS Inference Procedure

Input: Test samples $\{\mathbf{x}_i\}_{i=1}^{N_{\text{test}}}$, confidence threshold τ_{conf} , bank capacity K , refinement rate β
Output: Predictions $\{\hat{y}_i\}_{i=1}^{N_{\text{test}}}$
 Initialize memory bank $\mathcal{M}_c = \emptyset$ for each class c ;
 Initialize adaptive parameters $\mathbf{S} = \mathbf{1}$, $\Delta \mathbf{F} = \mathbf{0}$;
for each test sample \mathbf{x}_i **do**
 Extract visual features: $\mathbf{G}_i = g(\mathbf{x}_i)$;
 Refine semantic embeddings:
 $\mathbf{F}' = \mathcal{N}(\mathbf{S} \odot \mathbf{F} + \Delta \mathbf{F})$;
 Compute refined queries: $\mathbf{Q}' = \mathbf{F}' \mathbf{W}_Q$;
 Aggregate visual features:
 $\mathbf{R}_i = \text{Attention}(\mathbf{Q}', \mathbf{G}_i)$;
 Project to semantic space: $\mathbf{v}_i = f_{\text{skel}}(\mathbf{r}_{i,\text{global}})$;
 Compute prediction probabilities: \mathbf{p}_i using \mathbf{v}_i and \mathbf{F}' ;
 Predict label: $\hat{y}_i = \arg \max_c p_{i,c}$;
 Compute confidence: $\text{conf}_i = p_{i,\hat{y}_i}$;
if $\text{conf}_i > \tau_{\text{conf}}$ **then**
 Update memory bank $\mathcal{M}_{\hat{y}_i}$ with $(\mathbf{x}_i, \hat{y}_i, \text{conf}_i)$;
if $|\mathcal{M}_{\hat{y}_i}| > K$ **then**
 Remove sample with lowest confidence from $\mathcal{M}_{\hat{y}_i}$;
end
end
if $|\mathcal{M}| \geq B_{\min}$ **then**
 // Sufficient samples for refinement
 Sample class-balanced batch $\mathcal{B} \subset \mathcal{M}$;
 Compute refinement loss:
 $\mathcal{L}_{\text{adapt}} = -\frac{1}{|\mathcal{B}|} \sum_{(\mathbf{x}_j, \hat{y}_j) \in \mathcal{B}} \log p'_{j,\hat{y}_j}$;
 Update parameters: $\mathbf{S} \leftarrow \mathbf{S} - \beta \nabla_{\mathbf{S}} \mathcal{L}_{\text{adapt}}$;
 Update parameters:
 $\Delta \mathbf{F} \leftarrow \Delta \mathbf{F} - \beta \nabla_{\Delta \mathbf{F}} \mathcal{L}_{\text{adapt}}$;
end
end
return $\{\hat{y}_i\}_{i=1}^{N_{\text{test}}}$

Memory Bank \mathcal{M} to store a balanced set of high-confidence, pseudo-labeled test samples. As detailed in Algorithm 1, for each incoming sample \mathbf{x}_i , we compute its prediction probability distribution using the current refined semantic embeddings \mathbf{F}' :

$$p_{i,c} = \frac{\exp(\text{sim}(\mathbf{v}_i, \mathbf{f}'_c) / \tau)}{\sum_{j=1}^C \exp(\text{sim}(\mathbf{v}_i, \mathbf{f}'_j) / \tau)} \quad (14)$$

where \mathbf{v}_i is the global visual feature and \mathbf{f}'_c is the refined global text feature for class c .

The memory bank maintains at most K samples per class, preventing bias towards frequent classes. When a class's bank is full, new high-confidence samples replace those with the lowest confidence, progressively improving the quality of stored exemplars.

Refinement Objective. Using the curated samples in $\mathcal{M} = \bigcup_c \mathcal{M}_c$, we define the refinement loss as the cross-entropy

over the pseudo-labels:

$$\mathcal{L}_{\text{adapt}} = -\frac{1}{|\mathcal{B}|} \sum_{(\mathbf{x}_j, \hat{y}_j) \in \mathcal{B}} \log p'_{j, \hat{y}_j} \quad (15)$$

where p'_{j, \hat{y}_j} is the probability for sample \mathbf{x}_j from a balanced batch $\mathcal{B} \subset \mathcal{M}$, recomputed with the current adaptive parameters. These parameters are then updated via gradient descent:

$$\theta_{\text{adapt}} \leftarrow \theta_{\text{adapt}} - \beta \nabla_{\theta_{\text{adapt}}} \mathcal{L}_{\text{adapt}} \quad (16)$$

where β is the refinement learning rate. This selective optimization process refines the semantic embeddings to better align with the true test distribution, stabilizing adaptation and improving generalization to unseen classes.

3.5 GZSL Protocol Extension

In GZSL, the model must differentiate between seen and unseen classes. Inspired by OOD detection methods [55], [56], [57], we implement an entropy-based gating mechanism. We first calculate the predictive entropy for each test sample \mathbf{x}_i with respect to the *entire* set of class semantics $\mathcal{Y}_s \cup \mathcal{Y}_u$:

$$H(\mathbf{p}_i) = - \sum_{c=1}^C p_{i,c} \log p_{i,c}. \quad (17)$$

Using an entropy threshold δ tuned on a validation set, we triage samples: those with entropy below δ (low uncertainty) are classified as likely ‘seen’, while those above δ (high uncertainty) are deemed ‘unseen’. Following this separation, we classify each subset independently using only the corresponding ‘seen’ or ‘unseen’ class prototypes. This prevents the model from defaulting to high-confidence seen class predictions for unseen samples. The class-balanced memory bank is especially critical here, as it maintains distinct, high-quality representations for both seen and unseen classes, preventing feature drift and ensuring the refinement process remains robust.

Summary. Our DynaPURLS framework addresses the semantic drift challenge in zero-shot skeleton-based action recognition through: (1) multi-granularity semantic representations that capture transferable motion concepts, (2) adaptive partitioning and visual-semantic alignment that flexibly aligns features across modalities and establishes robust multi-scale correspondences, and (3) dynamic test-time feature refinement that adapts semantic embeddings and indirectly refines visual features, with entropy-based domain separation for robust GZSL performance. Together, these components enable effective knowledge transfer to unseen action classes while maintaining strong performance on seen classes.

4 EXPERIMENTS

4.1 Experimental Setup

4.1.1 Datasets

We evaluate our approach on three widely-used, large-scale benchmarks for skeleton-based action recognition to ensure a comprehensive assessment of its capabilities.

NTU RGB+D 60 [58] is a foundational dataset in the field, containing 56,880 skeleton sequences that cover 60

distinct action classes. These actions were performed by 40 different subjects and captured from 80 viewpoints, providing significant diversity. Each sequence offers 3D coordinates for 25 primary body joints and can accommodate up to two performers, with coordinate values being padded with zeros for single-person actions.

NTU RGB+D 120 [22] serves as a large-scale extension of its predecessor, significantly increasing the complexity and diversity with 114,480 samples across 120 action classes. The data was collected from a larger pool of 106 subjects and across 155 distinct viewpoints, presenting a more challenging scenario for generalization. It maintains the same 25-joint skeleton representation, making it directly comparable with NTU RGB+D 60.

PKU-MMD [30] is another critical multi-modal benchmark, comprising approximately 20,000 action instances that span 51 categories. A key feature of this dataset is its division into two phases of increasing difficulty (Phase I and II), allowing for evaluation under varying levels of challenge. Although it follows the same 25-joint skeleton format as the NTU RGB+D datasets, it introduces different action types and recording conditions, making it an excellent testbed for evaluating model robustness and cross-dataset generalization.

4.1.2 Evaluation Protocols

We conduct experiments under two standard protocols. In **Zero-Shot Learning (ZSL)**, the model is trained exclusively on seen classes and evaluated only on unseen classes, where we report Top-1 accuracy on the unseen test set. In **Generalized Zero-Shot Learning (GZSL)**, the model must distinguish between both seen and unseen classes during testing, presenting a more realistic but challenging scenario. For GZSL, we report accuracy for seen classes (S), unseen classes (U), and their harmonic mean ($H = \frac{2 \times S \times U}{S + U}$), where H provides a balanced measure of performance across both domains.

Following established practices [59], we employ multiple class split configurations to comprehensively assess generalization capability. For NTU RGB+D 60, we use 55/5 and 48/12 splits (seen/unseen classes), while NTU RGB+D 120 uses 110/10 and 96/24 splits. Additionally, recent works [26], [60] have introduced random split settings to provide more robust evaluation. For fair comparison, we adopt the same three public random splits from prior work for each dataset: three random 55/5 splits for NTU 60, three random 110/10 splits for NTU 120, and three random 46/5 splits for PKU-MMD, where we report averaged results across all random trials to ensure consistency with previous evaluations.

4.1.3 Baseline Methods

We compare against comprehensive state-of-the-art skeleton-based zero-shot learning methods spanning different paradigms. The embedding-based methods include DeVISE [61], which learns a linear transformation from visual to semantic space; ReViSE [62], which employs bidirectional projections between modalities; and JPoSE [40], which leverages part-of-speech embeddings for fine-grained action understanding. Among generative approaches, CADA-VAE [63] uses variational autoencoders to synthesize visual features

from semantic descriptions, while SynSE [59] exploits syntactic structures in action labels to guide feature generation.

Recent skeleton-specific methods have introduced specialized architectures. These include SMIE [60], which maximizes mutual information between visual and textual distributions; SA-DVAE [26], which employs disentangled autoencoders to separate action-specific features; STAR [27], which utilizes dual prompts guided by fine-grained information; Neuron [42], which introduces a framework for learning context-aware evolving representations; and SCoPLe [41], which pioneers semantic-guided cross-modal prompt learning. We also extend our PURLS [31] method to GZSL and other experimental settings to facilitate comprehensive evaluation and demonstrate the consistent improvements achieved by DynaPURLS across different scenarios.

4.1.4 Implementation Details

Our framework is meticulously implemented, building upon our proposed multi-granularity architecture with a novel dynamic inference-time refinement mechanism. The visual backbone is a **Shift-GCN** [64], which has proven effective for skeleton-based action recognition. It extracts rich 256-dimensional spatio-temporal features from input skeleton sequences through its efficient shift graph convolution and temporal convolution operations. Following the standard ZSL protocol to prevent any information leakage, we pre-train this visual encoder using only the seen class samples specific to each experimental split configuration [24]. All training parameters are kept consistent with those used in [24] and [60] to ensure fair comparison.

For the generation of semantic representations, we employ **GPT-3 (text-davinci-003)** language model. We use carefully engineered prompts to guide the model to produce detailed and structured action descriptions. These prompts systematically decompose each action into spatial components (covering 4 body parts: head, hands, torso, and legs) and temporal phases (across 3 segments: start, middle, and end). The resulting textual descriptions are then encoded into high-quality 512-dimensional feature vectors using the pre-trained **CLIP text encoder (ViT-B/32)**. The core of our adaptive alignment is the cross-modal attention mechanism, which employs learnable projection matrices $W_Q \in \mathbb{R}^{512 \times 150}$ and $W_K \in \mathbb{R}^{256 \times 150}$, with a shared hidden dimension of $h = 150$. The final visual representation is projected into the semantic space by a projection head, f_{skel} , which consists of a 2-layer MLP with 512 hidden units and ReLU activation functions.

Our training is configured for robust convergence. We use the Adam optimizer with a learning rate of $1e^{-4}$ and a batch size of 256. The model is trained for a maximum of 300 epochs, but we employ an early stopping strategy that halts training if the validation accuracy does not improve for 20 consecutive epochs. For data processing, sequences from the NTU datasets are processed with a length of $L = 300$ and $J = 25$ joints, accommodating up to $M = 2$ performers. For the PKU-MMD dataset, we follow the configuration from [65] with $J = 18$ joints.

At inference time, our dynamic refinement mechanism optimizes the lightweight affine transformation parameters S and $\Delta\mathcal{F}$. This is done using an Adam optimizer with a higher initial learning rate of 0.01, which is then decayed using

a cosine annealing schedule. The class-balanced memory bank, which is central to our method's stability, is configured to maintain up to $K = 16$ high-confidence samples per class, selected based on a confidence threshold of $\tau = 0.1$. Test batches use a size of 1 to mimic real online scenarios for efficient processing. All experiments reported were conducted on a single NVIDIA A100 GPU using PyTorch 1.12.

4.2 Comparison with State-of-the-Art

Our proposed method, DynaPURLS, achieves substantial and consistent improvements across nearly all datasets and evaluation settings, establishing a new state-of-the-art in skeleton-based zero-shot action recognition. The comprehensive results, presented in Table 3 for fixed splits and Table 4 for random splits, are detailed below.

In the standard ZSL setting (Table 3), DynaPURLS demonstrates a superior ability to generalize to unseen classes. On NTU RGB+D 60, we achieve 88.52% (55/5 split) and a remarkable 71.80% (48/12 split), surpassing the very strong recent competitor, Neuron, by 1.62% and 9.1%, respectively. The performance gains are even more pronounced on the larger NTU RGB+D 120 dataset. Here, we attain 89.06% (110/10 split) and 69.11% (96/24 split), outperforming the next-best methods (SCoPLe and Neuron) by significant margins of 14.53% and 12.01%. These improvements over the latest SOTA models underscore our method's enhanced capacity to transfer fine-grained motion patterns.

The GZSL setting provides a more practical evaluation, where our method excels by achieving the best harmonic mean (H) in three of the four challenging splits (Table 3). We achieve leading H-scores of 70.66% (NTU60 48/12), 81.49% (NTU120 110/10), and 64.36% (NTU120 96/24). These results represent improvements of up to 11.56% over the next-best competitors. While the NTU60 55/5 split presents a unique challenge due to severe class imbalance, where the limited number of unseen classes (only 5) causes our GZSL method to over-predict seen classes for unseen samples, thereby affecting the harmonic mean, our method consistently demonstrates state-of-the-art performance across the other three more balanced evaluation scenarios. This robust GZSL performance stems from our ability to drastically improve unseen class accuracy (U) while maintaining high seen class accuracy (S).

Finally, Table 4 validates our method's robustness on random class splits. DynaPURLS consistently outperforms all baselines. On NTU 60 and PKU-MMD, we improve the GZSL harmonic mean over the strong SCoPLe baseline by 1.77% and 5.26%, respectively. The most striking gains are on the large-scale NTU 120 dataset, where our ZSL and GZSL scores of 90.04% and 74.72% represent a massive leap of 36.7% and 20.64% over the previous SOTA (SCoPLe), solidifying the state-of-the-art status of our approach.

5 ABLATION STUDIES & QUALITATIVE ANALYSIS

To thoroughly understand the effectiveness of our approach and the contribution of each component, we conduct extensive ablation studies and qualitative analysis. This comprehensive evaluation reveals the effectiveness of individual components in both PURLS and DynaPURLS, as well as the underlying principles behind their success.

TABLE 3: Comparison with state-of-the-art methods on NTU RGB+D 60 and NTU RGB+D 120 under different splits. **ZSL Acc** denotes the Top-1 accuracy in the ZSL setting (highlighted in gray). **S**, **U**, and **H** denote the seen accuracy, unseen accuracy, and harmonic mean in the GZSL setting, respectively. **H** is highlighted in gray as the key metric. **Bold** indicates the best performance, underline indicates the second best.

Method	NTU RGB+D 60								NTU RGB+D 120							
	55/5 (1368 samples)				48/12 (3291 samples)				110/10 (4249 samples)				96/24 (9892 samples)			
	ZSL	S	U	H	ZSL	S	U	H	ZSL	S	U	H	ZSL	S	U	H
ReViSE [62]	53.91	74.22	34.73	47.32	17.49	62.36	20.77	31.16	55.04	48.69	44.84	46.68	32.38	49.66	25.06	33.31
JPoSE [40]	64.82	64.44	50.29	56.49	28.75	60.49	20.62	30.75	51.93	47.66	46.40	47.05	32.44	38.62	22.79	28.67
CADA-VAE [63]	76.84	69.38	61.79	65.37	28.96	51.32	27.03	35.41	59.53	47.16	49.78	48.44	35.77	41.11	34.14	37.31
SynSE [59]	75.81	61.27	56.93	59.02	33.30	52.21	27.85	36.33	62.69	52.51	57.60	54.94	38.70	56.39	32.25	41.04
SMIE [60]	77.98	-	-	-	40.18	-	-	65.74	-	-	-	45.30	-	-	-	-
STAR [27]	81.40	69.00	69.90	69.40	45.10	62.70	37.00	46.60	63.30	59.90	52.70	56.10	44.30	51.20	36.90	42.90
SA-DVAE [26]	82.37	62.28	70.80	66.27	41.38	50.20	36.94	42.56	68.77	61.10	59.75	60.42	46.12	58.82	35.79	44.50
Neuron [42]	86.90	69.10	73.80	71.40	62.70	61.60	56.80	59.10	71.50	67.60	59.50	63.30	57.10	67.50	44.40	53.60
SCoPLe [41]	84.10	69.60	71.94	70.75	52.96	54.49	61.83	57.93	74.53	63.51	61.08	62.27	52.17	53.33	51.18	52.24
PURLS [31]	79.22	71.70	60.35	65.53	40.99	81.60	36.92	50.84	71.95	76.25	67.89	72.00	52.01	72.67	45.32	<u>56.00</u>
DynaPURLS(Ours)	88.52	72.67	67.43	69.95	71.80	82.48	61.81	70.66	89.06	80.02	83.00	81.49	69.11	74.41	56.70	64.36

TABLE 4: Comparison with state-of-the-art methods on NTU RGB+D 60, NTU RGB+D 120, and PKU-MMD under three different random splits. **ZSL** denotes the Top-1 accuracy in the ZSL setting. **GZSL** denotes the harmonic mean in the GZSL setting.

Method	NTU 60		NTU 120		PKU-MMD	
	ZSL	GZSL	ZSL	GZSL	ZSL	GZSL
ReViSE [62]	60.94	60.34	44.90	40.34	59.34	49.82
JPoSE [40]	59.44	60.05	46.69	43.69	57.17	51.64
CADA-VAE [63]	61.84	66.38	45.15	45.64	60.74	45.75
SynSE [59]	64.19	67.47	47.28	43.47	53.85	49.47
SMIE [60]	65.08	-	46.40	-	60.83	-
SA-DVAE [31]	84.20	75.27	50.67	47.54	66.54	54.72
SCoPLe [41]	83.72	77.67	53.34	54.08	71.41	54.85
PURLS [31]	81.10	75.52	52.60	52.99	64.07	49.80
DynaPURLS(Ours)	86.75	79.44	90.04	74.72	78.26	60.11

5.1 Effect of Framework Universality

We first examine whether our multi-granularity alignment strategy generalizes across different visual backbones and language models. In this experiment, we compare our full model against a ‘**Global**’ baseline, which aligns globally-averaged visual features with simple class labels. We vary the skeleton encoders (AA-GCN, CTR-GCN, DG-GCN, PoseC3D, Shift-GCN) and the action descriptor generators (GPT-3, GPT-3.5, GPT-4), with results presented in Table 5.

The results demonstrate the robust generality of our approach. Our method achieves consistent and substantial performance gains, ranging from 10% to 20% in absolute accuracy over the global baseline, regardless of the architectural configuration. Notably, our framework successfully adapts to PoseC3D, which outputs 2D heatmap features rather than graph-structured data. While a static partitioning scheme would fail in this scenario, our adaptive attention mechanism naturally handles the different input structure by learning pixel-wise attention weights, validating the flexibility and universality of our design.

5.2 Effect of Semantic Enrichment and Partitioning

This study analyzes the impact of semantic representations and partitioning strategies on performance, both before and after applying our inference-time dynamic refinement. We evaluate four base strategies detailed in Table 6: ‘**Global**

TABLE 5: Ablation study on NTU RGB+D 60 (%) examining framework universality by replacing the skeleton encoder backbone or action descriptor generator.

Encoder	Descriptor	Model	NTU RGB+D 60	
			55/5	48/12
AA [66]	GPT3	Global	62.79	28.09
AA [66]	GPT3	Ours	76.75	32.39
CTR [67]	GPT3	Global	65.16	34.56
CTR [67]	GPT3	Ours	79.97	39.42
DG [20]	GPT3	Global	64.28	34.04
DG [20]	GPT3	Ours	80.41	41.06
PoseC3D [68]	GPT3	Global	63.45	35.71
PoseC3D [68]	GPT3	Ours	81.14	41.60
Shift	GPT3	Global	64.69	35.46
Shift	GPT3	Ours	79.23	40.99
Shift	GPT3.5	Global	66.49	38.01
Shift	GPT3.5	Ours	79.17	40.98
Shift	GPT4	Global	64.71	40.76
Shift	GPT4	Ours	81.53	41.90

(Original)’ using basic class names; ‘**Global (GPT-3)**’ using enriched semantic descriptions; ‘**Static**’ using predefined body-part partitions; and our ‘**Adaptive**’ strategy, where an attention mechanism dynamically identifies informative regions.

The base model results (rows without ‘✓’) show that richer semantics and finer-grained partitioning both provide substantial performance gains on their own. However, the table reveals a more critical insight into how these factors influence the effectiveness of our dynamic refinement. As indicated by the gains in parentheses, refinement consistently improves all models, but the magnitude of this improvement is highly dependent on the quality of the initial alignment.

The data clearly shows that the benefits of refinement are amplified by better initial features. The performance uplift for the ‘Global (GPT-3)’ model is significantly more substantial than for the ‘Global (Original)’ model, and this trend is even more pronounced with the partitioning strategy. Our ‘Adaptive’ model reaps remarkably larger rewards from refinement compared to the ‘Static’ model across all test cases. This demonstrates a powerful synergistic effect: our dynamic refinement is not a simple add-on, but a mechanism whose success is profoundly enhanced by the high-quality, discriminative features generated by our adaptive alignment.

TABLE 6: Ablation study (%) on different alignment strategies and the effect of inference-time dynamic refinement. The ‘Dynamic’ column indicates whether refinement is applied.

Strategy	Dynamic	NTU RGB+D 60		NTU RGB+D 120	
		55/5	48/12	110/10	96/24
Global (Original)	✓	64.69 71.82 (+7.13)	35.46 44.28 (+8.82)	66.96 73.05 (+6.09)	44.27 47.29 (+3.02)
Global (GPT-3)	✓	78.50 84.67 (+6.17)	33.47 53.05 (+19.58)	64.89 85.64 (+20.75)	47.15 52.77 (+5.62)
Static	✓	76.46 78.53 (+2.07)	33.03 36.80 (+3.77)	67.62 70.25 (+2.63)	46.83 48.08 (+1.25)
Adaptive	✓	79.23 88.52 (+9.29)	40.99 71.80 (+30.81)	71.95 89.06 (+17.11)	52.01 69.11 (+17.10)

approach.

5.3 Effect of Multi-Granularity Components

This experiment systematically evaluates the contributions of the body-part (BP) and temporal-interval (TI) alignment components, as shown in Table 7. We begin with a ‘Global-only’ baseline and progressively add the BP and TI components, testing both fixed (‘Average’) and ‘Learnable’ weighting strategies for aggregating their alignment losses. We then apply our inference-time dynamic ‘Refinement’ to each configuration.

The results before refinement show that both BP and TI components independently improve over the baseline, and their combination (‘BP’ + ‘TI’) yields the best initial results, confirming they capture complementary knowledge. A crucial distinction emerges after refinement: the BP component shows a stronger synergy with the refinement process, achieving higher accuracy than the TI component alone, especially on challenging splits. We attribute this to the fact that body-part descriptions (e.g., “left hand”) are more concrete and specific than abstract temporal descriptions (e.g., “initial phase”), providing more distinct and stable features for the model to disambiguate during the confidence-boosting refinement stage.

The substantial performance leap in all ‘Refinement’ rows highlights the efficacy of our two-stage approach. The initial multi-granularity training establishes a foundational but potentially low-confidence mapping, especially for visually similar actions. The subsequent dynamic refinement directly addresses this by minimizing prediction entropy. This process compels the model to increase its prediction confidence, effectively forcing it to discover a more discriminative and accurate alignment distribution that was implicitly learned but not fully expressed, leading to a significant improvement in final accuracy.

5.4 Effect of the Inference-Time Dynamic Refinement Framework

This study evaluates the core components of our dynamic refinement mechanism. We compare three configurations shown in Table 8: (1) the ‘Baseline’ static model without test-time refinement; (2) refinement using pseudo-labeling but ‘w/o Memory Bank’; and (3) our ‘Full Framework’, which includes the class-balanced memory bank.

The results demonstrate the critical role of the memory bank. While naive pseudo-labeling (‘w/o Memory Bank’) provides some benefit, it can be unstable and lead to limited gains. In contrast, our ‘Full Framework’ delivers consistent

TABLE 7: Ablation study (%) analyzing the contribution of body-part (BP) and temporal-interval (TI) alignment with different aggregation strategies, with and without inference-time refinement.

Method	BP	TI	NTU RGB+D 60		NTU RGB+D 120	
			55/5	48/12	110/10	96/24
Global-only			78.50	33.47	64.89	47.15
Average	✓		76.68	37.80	68.11	30.93
Learnable	✓		76.32	37.62	71.73	40.92
Refinement	✓		87.40	61.46	81.57	60.14
Average		✓	78.65	38.80	55.73	50.67
Learnable		✓	77.70	40.69	71.26	46.13
Refinement		✓	87.25	55.42	80.40	58.74
Average	✓	✓	79.02	39.92	73.55	51.38
Learnable	✓	✓	79.23	40.99	71.95	52.01
Refinement	✓	✓	88.52	71.80	89.06	69.11

TABLE 8: Ablation study (%) on test-time refinement components. Results show ZSL accuracy and GZSL harmonic mean.

Method	NTU RGB+D 60				NTU RGB+D 120			
	55/5 ZSL	48/12 ZSL	110/10 ZSL	96/24 ZSL	55/5 GZSL	48/12 GZSL	110/10 GZSL	96/24 GZSL
Baseline	79.22	64.35	40.99	48.74	71.95	72.97	52.01	53.99
w/o Memory Bank	78.02	63.83	51.60	56.99	81.20	77.09	59.82	56.95
Full Framework	88.52	69.95	71.80	70.66	89.06	81.49	69.11	64.36

and substantial improvements across all settings, including a 30.81% gain in ZSL accuracy on the NTU-60 48/12 split. This confirms that the class-balanced memory bank is essential for stabilizing the adaptation process, preventing the model from reinforcing incorrect predictions by maintaining a diverse set of high-quality adaptation samples.

5.5 Effect of Domain-Specific refinement in GZSL

To understand the impact of our test-time refinement in the GZSL setting, we analyze its effect on seen (S) and unseen (U) classes separately. Table 9 details the performance of the ‘Baseline’ model (no refinement), a ‘Partial’ model adapted only on seen class data, and our ‘Full’ approach that adapts on the entire test distribution.

The results reveal an important and desirable asymmetry. Our ‘Full’ refinement strategy primarily benefits the unseen classes, with accuracy gains of up to 24.89%, while performance on seen classes is preserved. This outcome supports our motivation that unseen classes suffer more from semantic drift and thus benefit most from refinement. Consequently, the harmonic mean (H) improves dramatically by up to 19.82%, demonstrating that our approach successfully mitigates bias towards seen classes and achieves a much better performance balance across both domains.

5.6 Effect of Alternative Adaptation Methods

To contextualize our contribution, we compare our dynamic refinement strategy against existing state-of-the-art TTA methods. For a fair comparison of the adaptation strategies themselves, all methods are applied to a frozen **PURLS** backbone. As shown in Table 10, our **DynaPURLS** achieves substantial improvements across all evaluation scenarios, with accuracy gains of 5.68% and 30.81% over the strongest baseline (TDA) on NTU-RGB+D 60, and 14.14% and 14.51% on NTU-RGB+D 120, demonstrating consistent superior performance.

TABLE 9: Analysis of test-time refinement impact on seen (S) and unseen (U) classes in GZSL, with harmonic mean (H).

Method	NTU RGB+D 60						NTU RGB+D 120											
	S	55/5	U	H	S	48/12	U	H	S	110/10	U	H	S	96/24	U	H		
Baseline	71.70	60.35	65.53	81.60	36.92	50.84	76.25	67.89	72.00	72.67	45.32	56.00						
Partial	72.67	60.35	65.93	82.48	36.92	51.01	80.02	67.89	73.46	74.41	45.32	56.33						
Full	72.67	67.43	69.95	82.48	61.81	70.66	80.02	83.00	81.49	74.41	56.70	64.36						

TABLE 10: Comparison with other TTA methods on NTU-RGB+D 60 and NTU-RGB+D 120 datasets.

Method	NTU-RGBD 60		NTU-RGBD 120		Throughput (samples/ms)
	55/5	48/12	110/10	96/24	
TPT [48]	40.11	27.98	22.10	17.10	0.70
AdaNPC [47]	81.77	42.52	72.50	53.16	2.15
CALIP [50]	80.02	45.10	72.27	51.84	2.48
TDA [51]	82.84	43.95	74.92	54.60	3.42
PURLS (baseline)	79.22	40.99	52.01	52.01	10.09
Ours (DynaPURLS)	88.52	71.80	89.06	69.11	1.95

Existing baselines exhibit significant limitations when applied to skeleton data. Gradient-based prompt tuning methods (TPT [48]) require iterative optimization that easily over-fits the small and highly imbalanced target streams characteristic of skeleton action recognition. Prototype and attention-based schemes (AdaNPC [47], CALIP [50]) compress each clip into a single holistic vector, discarding fine-grained joint dynamics and thus confusing actions that differ only in local motion patterns. While TDA [51] partially addresses these issues with a dual cache mechanism, it still operates at a single global scale and ignores temporal phase diversity, limiting its effectiveness for complex multi-phase actions.

In contrast, our method, **DynaPURLS**, introduces a paradigm of dynamic, confidence-guided alignment that specifically addresses these limitations. Instead of feature compression or direct backbone updates, it employs a lightweight transformation to refine textual features at multiple granularities, preserving both body-part specificity and temporal phase information. This confidence-guided optimization is critically stabilized by a class-balanced memory bank, which prevents bias towards dominant classes and ensures robust adaptation across imbalanced data streams, leading to the superior performance empirically demonstrated in the table.

5.7 Effect of Key Hyperparameters of our Refinement Framework

We analyze the model’s sensitivity to key hyperparameters of our refinement framework. Figure 7 presents the performance analysis on the NTU RGB+D dataset, revealing important trade-offs for optimal performance.

Confidence Threshold. The confidence threshold τ (panel a) acts as an initial filter for noisy samples. Performance improves as τ increases to 0.2 by selecting higher-quality samples, but declines sharply beyond this as misclassified samples dominate the refinement process. A lower initial τ is preferable, as our memory bank iteratively improves sample quality over time; an overly restrictive threshold hinders refinement and risks overfitting.

Memory Bank Capacity. The memory bank capacity K (panel b) introduces a critical trade-off. An overly small K limits sample diversity and risks overfitting, while an

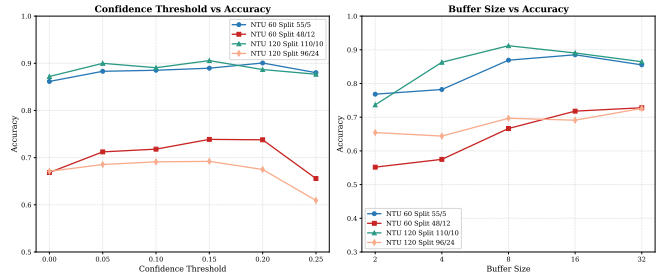


Fig. 7: Hyperparameter sensitivity analysis on NTU RGB+D dataset. (a) Effect of confidence threshold τ on refinement quality. (b) Impact of memory bank capacity K on performance.

excessively large K can be compromised by samples with incorrect pseudo-labels. This is reflected in the performance, which first increases and then declines as K grows. Our empirical results suggest that a capacity of $K \in [8, 16]$ strikes an optimal balance.

These results confirm that while our method is robust within reasonable parameter ranges, understanding these trade-offs is key to maximizing its performance.

5.8 Class-wise Performance Analysis

Figure 8 presents a detailed class-wise comparison between PURLS and DynaPURLS on the NTU RGB+D 120 dataset (96/24 split), revealing how our dynamic refinement mechanism affects different action categories. The most significant improvements occur in actions with distinctive motion patterns: “Cross hands” (+0.699), “Take off hat” (+0.659), and “Shake head” (+0.640), where clear visual signatures enable reliable confidence-based refinement. Conversely, actions like “OK sign” (-0.204) and “Hands up” (-0.188) show performance degradation, primarily due to visual ambiguity with similar gestures—for instance, “OK sign” can be confused with “Thumb up” when viewed from certain angles. Overall, DynaPURLS improves performance on 17 out of 24 unseen classes (70.8%), with an average gain of +0.308 for improved classes, demonstrating that our test-time refinement is particularly effective for actions with unambiguous motion patterns while highlighting the challenge of refining semantically similar actions as a direction for future work.

5.9 Confusion Matrix Analysis

Figure 9 compares confusion matrices before and after refinement with DynaPURLS for the NTU RGB+D 55/5 split. Before refinement, the model struggles to distinguish between similar actions, such as *reading* and *writing*, due to their overlapping upper-body poses, resulting in significant off-diagonal confusion. Post-refinement, the diagonal sharpens, and off-diagonal elements lighten, indicating that DynaPURLS enables differentiation of previously indistinguishable classes. However, this improvement introduces a trade-off: the model occasionally exhibits overconfidence, leading to misclassifications in some cases, as evidenced by residual off-diagonal elements.

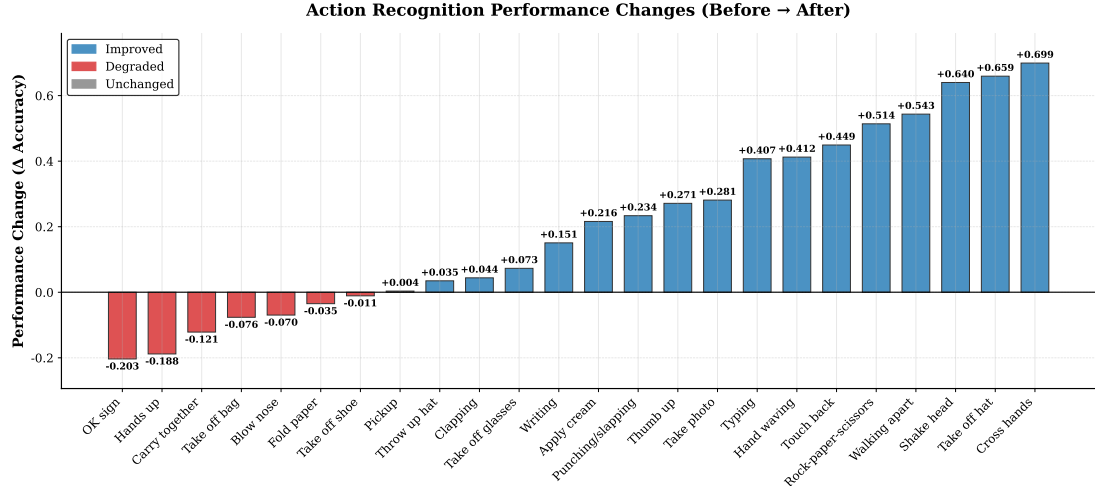


Fig. 8: Class-wise performance changes from PURLS to DynaPURLS on NTU RGB+D 120 (96/24 split). Actions are sorted by performance change, with blue bars indicating improvement, red bars indicating degradation, and gray indicating negligible change.

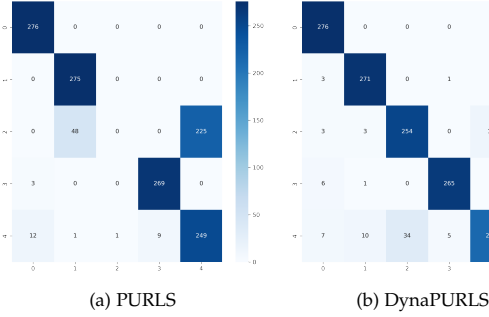


Fig. 9: Confusion matrices comparison for NTU RGB+D 55/5 split before and after refinement with DynaPURLS

5.10 Progressive Refinement Stages Analysis

Following the requirements of online test-time adaptation [48], [53], our framework processes each batch of samples with different parameters for feature refinement across sequential stages. To evaluate the impact of this progressive approach, we visualize feature distributions using t-SNE, dividing the test set into four parts according to the batch testing order, with each part corresponding to a specific stage. As shown in Fig. 10, the visual features from different classes exhibit significant overlap at Stage 1. With test-time feature refinement, Stage 2 achieves more distinct class boundaries and improved skeleton-text alignment, though overlap persists between two specific classes. In Stage 3, further refinement reduces this overlap, and by Stage 4, the overlapping issue is largely resolved, demonstrating the effectiveness of our progressive refinement strategy in aligning skeleton and text features.

6 DISCUSSION

While DynaPURLS achieves state-of-the-art performance across multiple benchmarks, our comprehensive analysis reveals several limitations that provide insights for future research directions.

Fine-grained Action Disambiguation. Our method exhibits reduced performance gains on certain action pairs that share highly similar motion patterns. As demonstrated in Figure 9,

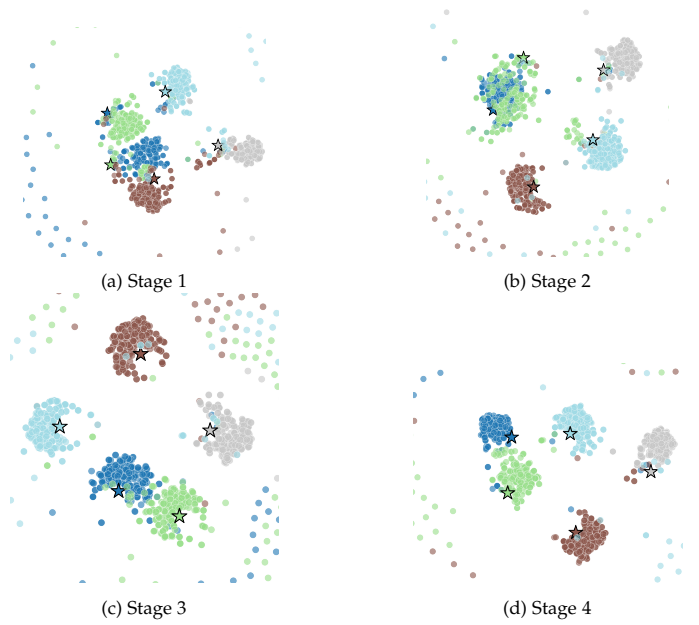


Fig. 10: t-SNE visualization of feature distributions during progressive refinement across inference stages on NTU-RGBD 60, where \star represents text features and \bullet represents skeleton features, with different colors denoting distinct classes, highlighting the improvement in class separability and skeleton-text alignment through DynaPURLS.

distinguishing between “writing” and “drawing” remains somewhat challenging, as both involve similar hand trajectories and differ primarily in subtle wrist movements and intent. Similarly, “brushing teeth” and “brushing hair” share comparable arm movements but differ in hand orientation and spatial location. These failure cases suggest that our multi-granularity semantic representations, while effective for most actions, may not capture the most discriminative features for extremely fine-grained distinctions. The confidence-guided refinement mechanism tends to converge to similar semantic adjustments for these ambiguous cases, limiting its effectiveness. Future work could explore adversarial training between confusing action pairs or develop attention mechanisms that automatically identify and emphasize the most

discriminative spatial-temporal regions for disambiguation. **Dataset Biases and Limited Generalization.** The current evaluation is confined to datasets collected in controlled indoor environments with specific demographic distributions. NTU RGB+D [11], [12] and PKU-MMD [30] predominantly feature young adults performing scripted actions in laboratory settings, which may not reflect the natural variability of human movements across different cultures, age groups, and real-world contexts. This controlled setting potentially inflates performance metrics and raises questions about generalization to in-the-wild scenarios where actions are performed with greater variability in speed, style, and environmental conditions. Addressing this limitation requires evaluation on more diverse datasets and development of domain adaptation techniques that can bridge the gap between controlled and naturalistic settings.

Memory Bank Reliability and Semantic Drift. While our class-balanced memory bank effectively stabilizes the refinement process, it relies on the assumption that high-confidence predictions correlate with correctness. However, our analysis reveals that the model can be confidently wrong, particularly for actions that are visually similar to well-represented seen classes. In such cases, the memory bank may accumulate systematically biased samples, potentially leading to semantic drift in the refined representations. This is especially problematic in the early stages of refinement when the initial predictions may be dominated by seen-class bias. Future methods could benefit from more sophisticated uncertainty estimation techniques, such as ensemble-based approaches or evidential deep learning, to distinguish between different types of uncertainty and identify truly reliable samples for refinement.

Temporal Dynamics and Sequential Dependencies. Our current approach treats temporal segments relatively independently through simple start-middle-end decomposition, which may not adequately capture the complex temporal dynamics inherent in human actions. Actions with variable-length phases or those requiring long-term dependencies are particularly affected by this limitation. The static temporal segmentation fails to adapt to the natural rhythm and pacing of different actions, potentially missing critical transitional movements that distinguish similar actions. Incorporating variable-length temporal segmentation or hierarchical temporal representations could better model the sequential nature of human movements and improve recognition of actions with complex temporal structures.

These limitations not only highlight areas for improvement but also underscore the challenging nature of zero-shot skeleton-based action recognition. Addressing these issues will be crucial for developing more robust and generalizable systems capable of understanding human actions in their full complexity and diversity across different populations and real-world scenarios.

7 CONCLUSION

In this paper, we introduced DynaPURLS, a novel framework that advances zero-shot skeleton-based action recognition through multi-granularity semantic alignment and dynamic test-time refinement. Our approach leverages LLM-generated hierarchical descriptions and adaptive cross-modal attention

to establish fine-grained visual-semantic correspondences that capture transferable motion patterns between seen and unseen action classes. To overcome the limitations of static representations, we pioneered the first test-time adaptation mechanism specifically designed for skeleton-based zero-shot learning, which dynamically refines semantic embeddings through confidence-guided optimization stabilized by a class-balanced memory bank. Extensive experiments on NTU RGB+D 60/120 and PKU-MMD datasets demonstrate substantial improvements over state-of-the-art methods, with particularly strong performance in the challenging GZSL setting where our method effectively balances recognition of both seen and unseen classes.

REFERENCES

- [1] I. Armeni, O. Sener, A. R. Zamir, H. Jiang, I. Brilakis, M. Fischer, and S. Savarese, "3d semantic parsing of large-scale indoor spaces," in *Proceedings of the IEEE Conference on Computer Vision and Pattern Recognition (CVPR)*, June 2016.
- [2] T. Vu, K. Kim, T. M. Luu, X. T. Nguyen, and C. D. Yoo, "Softgroup for 3d instance segmentation on point clouds," 2022.
- [3] Y. Li, A. W. Yu, T. Meng, B. Caine, J. Ngiam, D. Peng, J. Shen, B. Wu, Y. Lu, D. Zhou, Q. V. Le, A. Yuille, and M. Tan, "Deepfusion: Lidar-camera deep fusion for multi-modal 3d object detection," 2022.
- [4] T. Yin, X. Zhou, and P. Krahenbuhl, "Center-based 3d object detection and tracking," in *Proceedings of the IEEE/CVF Conference on Computer Vision and Pattern Recognition (CVPR)*, June 2021, pp. 11784–11793.
- [5] C. Zhu, Q. Jia, W. Chen, Y. Guo, and Y. Liu, "Deep learning for video-text retrieval: a review," *International Journal of Multimedia Information Retrieval*, vol. 12, no. 1, p. 3, 2023.
- [6] C. Wojek, S. Walk, S. Roth, and B. Schiele, "Monocular 3d scene understanding with explicit occlusion reasoning," in *2011 IEEE Conference on Computer Vision and Pattern Recognition (CVPR)*, 06 2011, pp. 1993–2000.
- [7] C. Cadena, A. Dick, and I. Reid, "Multi-modal auto-encoders as joint estimators for robotics scene understanding," in *Robotics: Science and Systems XII*, 06 2016.
- [8] D. Tran, H. Wang, L. Torresani, J. Ray, Y. LeCun, and M. Paluri, "A closer look at spatiotemporal convolutions for action recognition," in *CVPR*. Computer Vision Foundation / IEEE Computer Society, 2018, pp. 6450–6459. [Online]. Available: http://openaccess.thecvf.com/content_cvpr_2018/html/Tran_A_Closer_Look_CVPR_2018_paper.html
- [9] B. Parsa, A. Narayanan, and B. Dariush, "Spatio-temporal pyramid graph convolutions for human action recognition and postural assessment," in *IEEE/CVF Winter Conference on Applications of Computer Vision*. IEEE, 2020, pp. 1069–1079. [Online]. Available: <https://doi.org/10.1109/WACV45572.2020.9093368>
- [10] Z. Cao, G. Hidalgo Martinez, T. Simon, S. Wei, and Y. A. Sheikh, "Openpose: Realtime multi-person 2d pose estimation using part affinity fields," *IEEE Transactions on Pattern Analysis and Machine Intelligence*, 2019.
- [11] A. Shahroudy, J. Liu, T.-T. Ng, and G. Wang, "Ntu rgb+d: A large scale dataset for 3d human activity analysis," in *2016 IEEE Conference on Computer Vision and Pattern Recognition (CVPR)*, 2016, pp. 1010–1019.
- [12] J. Liu, A. Shahroudy, M. Perez, G. Wang, L.-Y. Duan, and A. C. Kot, "Ntu rgb+ d 120: A large-scale benchmark for 3d human activity understanding," *IEEE transactions on pattern analysis and machine intelligence*, vol. 42, no. 10, pp. 2684–2701, 2019.
- [13] M. Rashmi and R. M. R. Guddeti, "Skeleton based human action recognition for smart city application using deep learning," in *2020 international conference on communication systems & networks (COMSNETS)*. IEEE, 2020, pp. 756–761.
- [14] Y. Zhang, Y. Tian, P. Wu, and D. Chen, "Application of skeleton data and long short-term memory in action recognition of children with autism spectrum disorder," *Sensors*, vol. 21, no. 2, p. 411, 2021. [Online]. Available: <https://doi.org/10.3390/s21020411>

[15] Q. Pham, D. Nguyen, T. Nguyen, T. N. Nguyen, D. Nguyen, D. Pham, T. Tran, T. Le, and H. Vu, "A study on skeleton-based action recognition and its application to physical exercise recognition," in *The 11th International Symposium on Information and Communication Technology, SoICT 2022*, Hanoi, Vietnam, December 1-3, 2022. ACM, 2022, pp. 239–246. [Online]. Available: <https://doi.org/10.1145/3568562.3568639>

[16] Y. Cao, C. Liu, Z. Huang, Y. Sheng, and Y. Ju, "Skeleton-based action recognition with temporal action graph and temporal adaptive graph convolution structure," *Multimedia Tools and Applications*, vol. 80, no. 19, pp. 29 139–29 162, 2021. [Online]. Available: <https://doi.org/10.1007/s11042-021-11136-z>

[17] Q. Nie and Y. Liu, "View transfer on human skeleton pose: Automatically disentangle the view-variant and view-invariant information for pose representation learning," *IJCV*, vol. 129, no. 1, pp. 1–22, 2021. [Online]. Available: <https://doi.org/10.1007/s11263-020-01354-7>

[18] M. Li, S. Chen, X. Chen, Y. Zhang, Y. Wang, and Q. Tian, "Actional-structural graph convolutional networks for skeleton-based action recognition," in *CVPR*. Computer Vision Foundation / IEEE, 2019, pp. 3595–3603. [Online]. Available: http://openaccess.thecvf.com/content_CVPR_2019/html/Li_Actional-Structural_Graph_Convolutional_Networks_for_Skeleton-Based_Action_Recognition_CVPR_2019_paper.html

[19] L. Shi, Y. Zhang, J. Cheng, and H. Lu, "Two-stream adaptive graph convolutional networks for skeleton-based action recognition," in *CVPR*. Computer Vision Foundation / IEEE, 2019, pp. 12 026–12 035. [Online]. Available: http://openaccess.thecvf.com/content_CVPR_2019/html/Shi_Two-Stream_Adaptive_Graph_Convolutional_Networks_for_Skeleton-Based_Action_Recognition_CVPR_2019_paper.html

[20] —, "Skeleton-based action recognition with directed graph neural networks," in *CVPR*. Computer Vision Foundation / IEEE, 2019, pp. 7912–7921. [Online]. Available: http://openaccess.thecvf.com/content_CVPR_2019/html/Shi_Skeleton-Based_Action_Recognition_With_Directed_Graph_Neural_Networks_CVPR_2019_paper.html

[21] K. Cheng, Y. Zhang, X. He, W. Chen, J. Cheng, and H. Lu, "Skeleton-based action recognition with shift graph convolutional network," in *2020 IEEE/CVF Conference on Computer Vision and Pattern Recognition (CVPR)*, 2020, pp. 180–189.

[22] J. Liu, A. Shahroudny, M. Perez, G. Wang, L.-Y. Duan, and A. C. Kot, "Ntu rgbd 120: A large-scale benchmark for 3d human activity understanding," *IEEE transactions on pattern analysis and machine intelligence*, vol. 42, no. 10, pp. 2684–2701, 2019.

[23] M. Wray, G. Csurka, D. Larlus, and D. Damen, "Fine-grained action retrieval through multiple parts-of-speech embeddings," in *2019 IEEE/CVF International Conference on Computer Vision (ICCV)*, 2019, pp. 450–459.

[24] P. Gupta, D. Sharma, and R. K. Sarvadevabhatla, "Syntactically guided generative embeddings for zero-shot skeleton action recognition," in *2021 IEEE International Conference on Image Processing (ICIP)*, 2021, pp. 439–443.

[25] Y. Zhou, W. Qiang, A. Rao, N. Lin, B. Su, and J. Wang, "Zero-shot skeleton-based action recognition via mutual information estimation and maximization," in *Proceedings of the 31st ACM International Conference on Multimedia, MM 2023*, Ottawa, ON, Canada, 29 October 2023– 3 November 2023, A. El-Saddik, T. Mei, R. Cucchiara, M. Bertini, D. P. T. Vallejo, P. K. Atrey, and M. S. Hossain, Eds. ACM, 2023, pp. 5302–5310. [Online]. Available: <https://doi.org/10.1145/3581783.3611888>

[26] S.-W. Li, Z.-X. Wei, W.-J. Chen, Y.-H. Yu, C.-Y. Yang, and J. Y. Jen Hsu, "Sa-dvae: Improving zero-shot skeleton-based action recognition by disentangled variational autoencoders," 2024. [Online]. Available: <https://arxiv.org/abs/2407.13460>

[27] Y. Chen, J. Guo, T. He, and L. Wang, "Fine-grained side information guided dual-prompts for zero-shot skeleton action recognition," 2024. [Online]. Available: <https://arxiv.org/abs/2404.07487>

[28] T. B. Brown, B. Mann, N. Ryder, M. Subbiah, J. Kaplan, P. Dhariwal, A. Neelakantan, P. Shyam, G. Sastry, A. Askell, S. Agarwal, A. Herbert-Voss, G. Krueger, T. Henighan, R. Child, A. Ramesh, D. M. Ziegler, J. Wu, C. Winter, C. Hesse, M. Chen, E. Sigler, M. Litwin, S. Gray, B. Chess, J. Clark, C. Berner, S. McCandlish, A. Radford, I. Sutskever, and D. Amodei, "Language models are few-shot learners," 2020.

[29] A. Radford, J. W. Kim, C. Hallacy, A. Ramesh, G. Goh, S. Agarwal, G. Sastry, A. Askell, P. Mishkin, J. Clark, G. Krueger, and I. Sutskever, "Learning transferable visual models from natural language supervision," 2021.

[30] L. Chunhui, H. Yueyu, L. Yanghao, S. Sijie, and L. Jiaying, "Pku-mmdb: A large scale benchmark for continuous multi-modal human action understanding," *arXiv preprint arXiv:1703.07475*, 2017.

[31] A. Zhu, Q. Ke, M. Gong, and J. Bailey, "Part-aware unified representation of language and skeleton for zero-shot action recognition," 2024. [Online]. Available: <https://arxiv.org/abs/2406.13327>

[32] L. Zhang, T. Xiang, and S. Gong, "Learning a deep embedding model for zero-shot learning," 2019.

[33] A. Lazaridou, G. Dinu, and M. Baroni, "Hubness and pollution: Delving into cross-space mapping for zero-shot learning," in *Proceedings of the 53rd Annual Meeting of the Association for Computational Linguistics and the 7th International Joint Conference on Natural Language Processing (Volume 1: Long Papers)*. Beijing, China: Association for Computational Linguistics, 07 2015, pp. 270–280.

[34] G. Dinu, A. Lazaridou, and M. Baroni, "Improving zero-shot learning by mitigating the hubness problem," 2015.

[35] E. Kodirov, T. Xiang, and S. Gong, "Semantic autoencoder for zero-shot learning," 2017.

[36] Z. Chen, Y. Luo, R. Qiu, S. Wang, Z. Huang, J. Li, and Z. Zhang, "Semantics disentangling for generalized zero-shot learning," 2021.

[37] S. Chen, Z. Hong, G.-S. Xie, W. Yang, Q. Peng, K. Wang, J. Zhao, and X. You, "Msdn: Mutually semantic distillation network for zero-shot learning," 2022.

[38] L. Xue, M. Gao, C. Xing, R. Martín-Martín, J. Wu, C. Xiong, R. Xu, J. C. Niebles, and S. Savarese, "Ulip: Learning a unified representation of language, images, and point clouds for 3d understanding," 2023.

[39] R. Zhang, Z. Guo, W. Zhang, K. Li, X. Miao, B. Cui, Y. Qiao, P. Gao, and H. Li, "Pointclip: Point cloud understanding by clip," in *Proceedings of the IEEE/CVF Conference on Computer Vision and Pattern Recognition (CVPR)*, June 2022, pp. 8552–8562.

[40] M. Wray, D. Larlus, G. Csurka, and D. Damen, "Fine-grained action retrieval through multiple parts-of-speech embeddings," in *Proceedings of the IEEE/CVF international conference on computer vision*, 2019, pp. 450–459.

[41] A. Zhu, J. Zhu, J. Bailey, M. Gong, and Q. Ke, "Semantic-guided cross-modal prompt learning for skeleton-based zero-shot action recognition," in *Proceedings of the Computer Vision and Pattern Recognition Conference (CVPR)*, June 2025, pp. 13 876–13 885.

[42] Y. Chen, J. Guo, S. Guo, and D. Tao, "Neuron: Learning context-aware evolving representations for zero-shot skeleton action recognition," 2024. [Online]. Available: <https://arxiv.org/abs/2411.11288>

[43] S. Niu, J. Wu, Y. Zhang, Y. Chen, S. Zheng, P. Zhao, and M. Tan, "Efficient test-time model adaptation without forgetting," in *International conference on machine learning*. PMLR, 2022, pp. 16 888–16 905.

[44] D. Wang, E. Shelhamer, S. Liu, B. Olshausen, and T. Darrell, "Tent: Fully test-time adaptation by entropy minimization," *arXiv preprint arXiv:2006.10726*, 2020.

[45] T. Gong, J. Jeong, T. Kim, Y. Kim, J. Shin, and S.-J. Lee, "Note: Robust continual test-time adaptation against temporal correlation," *Advances in Neural Information Processing Systems*, vol. 35, pp. 27 253–27 266, 2022.

[46] Q. Wang, O. Fink, L. Van Gool, and D. Dai, "Continual test-time domain adaptation," in *Proceedings of the IEEE/CVF Conference on Computer Vision and Pattern Recognition*, 2022, pp. 7201–7211.

[47] Y. Zhang, X. Wang, K. Jin, K. Yuan, Z. Zhang, L. Wang, R. Jin, and T. Tan, "Adanpc: Exploring non-parametric classifier for test-time adaptation," in *International conference on machine learning*. PMLR, 2023, pp. 41 647–41 676.

[48] M. Shu, W. Nie, D.-A. Huang, Z. Yu, T. Goldstein, A. Anandkumar, and C. Xiao, "Test-time prompt tuning for zero-shot generalization in vision-language models," *Advances in Neural Information Processing Systems*, vol. 35, pp. 14 274–14 289, 2022.

[49] C.-M. Feng, K. Yu, Y. Liu, S. Khan, and W. Zuo, "Diverse data augmentation with diffusions for effective test-time prompt tuning," 2023. [Online]. Available: <https://arxiv.org/abs/2308.06038>

[50] Z. Guo, R. Zhang, L. Qiu, X. Ma, X. Miao, X. He, and B. Cui, "Calip: Zero-shot enhancement of clip with parameter-free attention," 2022. [Online]. Available: <https://arxiv.org/abs/2209.14169>

[51] A. Karmanov, D. Guan, S. Lu, A. El Saddik, and E. Xing, "Efficient test-time adaptation of vision-language models," in *Proceedings*

of the IEEE/CVF Conference on Computer Vision and Pattern Recognition, 2024, pp. 14 162–14 171.

[52] F. Pourpanah, M. Abdar, Y. Luo, X. Zhou, R. Wang, C. P. Lim, X.-Z. Wang, and Q. J. Wu, “A review of generalized zero-shot learning methods,” *IEEE transactions on pattern analysis and machine intelligence*, vol. 45, no. 4, pp. 4051–4070, 2022.

[53] M. Zhang, S. Levine, and C. Finn, “Memo: Test time robustness via adaptation and augmentation,” 2022. [Online]. Available: <https://arxiv.org/abs/2110.09506>

[54] A. van den Oord, Y. Li, and O. Vinyals, “Representation learning with contrastive predictive coding,” *Corr*, vol. abs/1807.03748, 2018. [Online]. Available: <http://arxiv.org/abs/1807.03748>

[55] Y. Yuan, R. He, Y. Dong, Z. Han, and Y. Yin, “Discriminability-driven channel selection for out-of-distribution detection,” in *Proceedings of the IEEE/CVF Conference on Computer Vision and Pattern Recognition*, 2024, pp. 26 171–26 180.

[56] Z. Gao, X.-Y. Zhang, and C.-L. Liu, “Unified entropy optimization for open-set test-time adaptation,” in *Proceedings of the IEEE/CVF Conference on Computer Vision and Pattern Recognition (CVPR)*, June 2024, pp. 23 975–23 984.

[57] R. Chan, M. Rottmann, and H. Gottschalk, “Entropy maximization and meta classification for out-of-distribution detection in semantic segmentation,” in *Proceedings of the ieee/cvf international conference on computer vision*, 2021, pp. 5128–5137.

[58] A. Shahroudy, J. Liu, T.-T. Ng, and G. Wang, “Ntu rgbd: A large scale dataset for 3d human activity analysis,” in *Proceedings of the IEEE conference on computer vision and pattern recognition*, 2016, pp. 1010–1019.

[59] P. Gupta, D. Sharma, and R. K. Sarvadevabhatla, “Syntactically guided generative embeddings for zero-shot skeleton action recognition,” 2021. [Online]. Available: <https://arxiv.org/abs/2101.11530>

[60] Y. Zhou, W. Qiang, A. Rao, N. Lin, B. Su, and J. Wang, “Zero-shot skeleton-based action recognition via mutual information estimation and maximization,” in *Proceedings of the 31st ACM International Conference on Multimedia*, ser. MM ’23. ACM, Oct. 2023, p. 5302–5310. [Online]. Available: <http://dx.doi.org/10.1145/3581783.3611888>

[61] A. Frome, G. S. Corrado, J. Shlens, S. Bengio, J. Dean, M. A. Ranzato, and T. Mikolov, “Devise: A deep visual-semantic embedding model,” in *Advances in Neural Information Processing Systems*, C. Burges, L. Bottou, M. Welling, Z. Ghahramani, and K. Weinberger, Eds., vol. 26. Curran Associates, Inc., 2013. [Online]. Available: https://proceedings.neurips.cc/paper_files/paper/2013/file/7cce53cf90577442771720a370c3c723-Paper.pdf

[62] Y.-H. Hubert Tsai, L.-K. Huang, and R. Salakhutdinov, “Learning robust visual-semantic embeddings,” in *Proceedings of the IEEE International conference on Computer Vision*, 2017, pp. 3571–3580.

[63] E. Schonfeld, S. Ebrahimi, S. Sinha, T. Darrell, and Z. Akata, “Generalized zero-shot learning via aligned variational autoencoders,” in *Proceedings of the IEEE/CVF Conference on Computer Vision and Pattern Recognition Workshops*, 2019, pp. 54–57.

[64] K. Cheng, Y. Zhang, X. He, W. Chen, J. Cheng, and H. Lu, “Skeleton-based action recognition with shift graph convolutional network,” in *Proceedings of the IEEE/CVF conference on computer vision and pattern recognition*, 2020, pp. 183–192.

[65] S. Yan, Y. Xiong, and D. Lin, “Spatial temporal graph convolutional networks for skeleton-based action recognition,” 2018.

[66] L. Shi, Y. Zhang, J. Cheng, and H. Lu, “Skeleton-based action recognition with multi-stream adaptive graph convolutional networks,” *IEEE Transactions on Image Processing*, vol. 29, pp. 9532–9545, 2020.

[67] Y. Chen, Z. Zhang, C. Yuan, B. Li, Y. Deng, and W. Hu, “Channel-wise topology refinement graph convolution for skeleton-based action recognition,” in *Proceedings of the IEEE/CVF International Conference on Computer Vision*, 2021, pp. 13 359–13 368.

[68] H. Duan, Y. Zhao, K. Chen, D. Lin, and B. Dai, “Revisiting skeleton-based action recognition,” *arXiv preprint arXiv:2104.13586*, 2021.



Jingmin Zhu received his Bachelor’s degree in Physics from Southern University of Science and Technology, Shenzhen, China, in July 2023, and his Master’s degree in Artificial Intelligence from Monash University, Melbourne, Australia, in July 2025. His current research interests include computer vision, multimodal large language models, domain adaptation, zero-shot learning, and few-one-shot learning.



Anqi Zhu received her Bachelor’s degree in Software Engineering from the University of New South Wales, Sydney, Australia, in 2021, and her Ph.D. degree in Engineering & IT from the University of Melbourne, Melbourne, Australia, in 2025. She subsequently joined Monash University, Melbourne, Australia, as a researcher in February 2025. Her current research interests include computer vision, skeleton-based action recognition, zero-shot learning, and few-one-shot learning.



James Bailey is a Professor in the Faculty of Engineering and Information Technology at The University of Melbourne and Program Lead for artificial intelligence. He was previously an Australian Research Council Future Fellow and is a researcher in the field of machine learning and artificial intelligence, including interdisciplinary applications and operational frameworks. His interests particularly relate to the assurance, certification and safety of systems based on machine learning and artificial intelligence. He works on the deployment of AI systems in collaboration with a wide range of industry and government partners across the defence, energy and health sectors.



Jun Liu is a Professor at School of Computing and Communications in Lancaster University. He got the PhD degree from Nanyang Technological University in 2019. He was with Singapore University of Technology and Design from 2019 to 2024. He is a Senior Area Editor of *IEEE Transactions on Image Processing*, and an Associate Editor of *IEEE Transactions on Circuits and Systems for Video Technology*, *IEEE Transactions on Neural Networks and Learning Systems*, *IEEE Transactions on Industrial Informatics*, *ACM Computing Surveys*, and *Pattern Recognition*. He is General Chair of BMVC 2026 and Program Chair of BMVC 2025. He has served as an Area Chair of CVPR, ECCV, ICML, NeurIPS, ICLR, IJCAI, AAAI, WACV, and MM. His research interests include computer vision, machine learning and digital health.



Hossein Rahmani received the PhD degree from the University of Western Australia, Perth, WA, Australia, in 2016. He is a professor with the School of Computing and Communications, Lancaster University in the U.K. Before that, he was a research fellow with the School of Computer Science and Software Engineering, University of Western Australia. His research interests include computer vision, action recognition, pose estimation, and deep learning. He now serves as an associate editor for IEEE Transactions On Neural Networks And Learning Systems (TNNLS), Pattern Recognition (PR) and ACM Computing Surveys, an Area Chair for NeurIPS 2025. Before that, he served as an Area Chair for CVPR 2024-2025, ICLR 2024-2025 and ECCV 2024, and a Senior Program Committee member of IJCAI 2023-2024.



Mohammed Bennamoun is Winthrop Professor in the Department of Computer Science and Software Engineering at UWA and is a researcher in computer vision, machine/deep learning, robotics, and signal/speech processing. He has published 4 books (available on Amazon), 1 edited book, 1 Encyclopedia article, 14 book chapters, 180+ journal papers, 260+ conference publications, 16 invited & keynote publications. His h-index is 79 and his number of citations is 36,000+ (Google Scholar). He was awarded 65+ competitive research grants, from the Australian Research Council, and numerous other Government, UWA and industry Research Grants. He successfully supervised 30+ PhD students to completion. He won the Best Supervisor of the Year Award at QUT (1998), and received award for research supervision at UWA (2008 & 2016) and Vice-Chancellor Award for mentorship (2016). He delivered conference tutorials at major conferences, including: IEEE Computer Vision and Pattern Recognition (CVPR 2016), Interspeech 2014, IEEE International Conference on Acoustics Speech and Signal Processing (ICASSP) and European Conference on Computer Vision (ECCV). He was also invited to give a Tutorial at an International Summer School on Deep Learning (DeepLearn 2017). He received Outstanding Paper Awards for his publications in IEEE Computational Intelligence Magazine and the Proceedings of the IEEE.



Farid Boussaid received the M.S. and Ph.D. degrees in microelectronics from the National Institute of Applied Science, Toulouse, France, in 1996 and 1999, respectively. He joined Edith Cowan University, Perth, Australia, as a Post-Doctoral Research Fellow; and the Visual Information Processing Research Group, as a member, in 2000. He joined The University of Western Australia, Crawley, Australia, in 2005, where he is currently a Professor. His current research interests include smart CMOS sensors, computer vision, and machine learning.



QiuHong Ke is a lecturer (assistant professor) with the Faculty of Information Technology, Monash University. Previously, she was a post-doctoral researcher with Max Planck Institute for Informatics from 2018 to 2019 and a lecturer with the University of Melbourne from 2020 to 2022. Her research interests include machine learning and computer vision.